Hindawi
Advances in Civil Engineering
Volume 2024, Article ID 7529543, 10 pages
https://doi.org/10.1155/2024/7529543

Research Article

Effects of Different Ratios of Fly Ash and River Sand on Mechanical Properties of Cemented Paste Backfill Materials

Jiang Li, Shenggen Cao, Yang Liu, Chiyuan Che, Changzheng Zhao, Shuyu Du, Kaifei Wang, and Ruiting Ma

State Key Laboratory for Fine Exploration and Intelligent Development of Coal Resources, School of Mines, China University of Mining and Technology, Xuzhou 221116, China

Correspondence should be addressed to Shenggen Cao; caoshenggencumt@163.com

Received 6 November 2023; Revised 2 December 2023; Accepted 9 December 2023; Published 2 January 2024

Academic Editor: Qianqian Wang

The mechanical properties of cemented paste backfill (CPB) are crucial for stope safety. Some mining areas in the Yellow River basin face a shortage of coal gangue, and these areas have abundant river sand (RS) resources. The use of RS as a fine aggregate can optimize the particle gradation of the material and improve the strength of the material. The effects of different fly ash (FA) and RS ratios on uniaxial compressive strength (UCS), elastic modulus, and microstructure of CPB were studied using uniaxial compression test and scanning electron microscopy. The results showed that with increasing FA content, UCS gradually increased at 7 and 14 days of CPB. However, at 28 days, the UCS of CPB first increased and then decreased. When the FA content was 40%, UCS at 28 days of backfill material reached its highest value of 14.76 MPa. The elastic modulus decreased as FA content increased and reached its maximum value of 1.54 GPa when FA content was 40%. FA optimized particle composition, promoted hydration reaction, and improved CPB strength; however, when FA content was more than 40%, it hindered cement hydration, thus deteriorating UCS. Based on Weibull distribution and prepeak correction factor, a damage constitutive model was established to describe the stress–strain process of CPB under load. The results of this research will provide a theoretical and experimental basis for CPB engineering design.

1. Introduction

Traditional coal mining methods have been associated with various environmental challenges and ecological impacts, including surface subsidence [1–4], groundwater loss [5–7], land desertification, and other problems. In addition, the accumulation of a large amount of coal gangue (CG) on the ground reduces land resources and causes environmental pollution [8–10]. The use of CG, fly ash (FA), and other solid waste materials to produce cemented paste backfill (CPB) material is an effective strategy for managing the goaf stability, controlling the movement of overlying strata, and reducing surface settlement. Such a strategy can also promote the recycling of solid waste resources, including CG and FA, and reduce environmental pollution caused by solid waste [11–13].

CPB usually comprises tailings, slag, excavation waste rock, CG, FA, and other solid waste materials with binder and water mixed in a certain proportion [14–16]. Feng et al. [17] studied the mechanical properties and failure characteristics of cement–gangue–fly ash backfill material (CGFB) under different FA and cement ratio conditions (F/C) using cement, CG, and FA as raw materials. The brittleness of CGFB decreased with the increase in F/C. The optimum design range of F/C was 0.5–2, and the strength limit of CGFB was 15.35 MPa. Yin et al. [18] used cement, waste rock, and FA as raw materials to produce cemented waste rock–FA backfill (CWFB) and investigated the slump, bleeding rate, and uniaxial compressive strength (UCS) of CWFB under different FA ratios, solid concentrations, and cement-sand ratios. The result showed that FA significantly improved the grading of coarse aggregate, and the grading coefficient of the mixture decreased from 0.45 to 0.31. The short-term strength (3–7 days) of CWFB increased with the increase in FA content, while the long-term strength and slump initially increased and then decreased. Sun et al. [19] used cement, CG, slag, and FA as raw materials to produce paste backfill materials. They analyzed the effects of solid mass

concentration, fine gangue ratio, and FA ratio on the fluidity and mechanical properties of paste backfill materials. The optimal ratio was as follows: solid mass concentration was 79.65%, where FA and fine gangue accounted for 15.67% and 57.19% of total mass, respectively. Fu et al. [20] used white cement, tailings, and FA as raw materials to study the early hydration process of the backfill body using low-field nuclear magnetic resonance, uniaxial compression test, and scanning electron microscopy (SEM) test. The results showed that the appropriate proportion of FA (10%) reduced the porosity of the backfill material, and excessive FA reduced the gelling product, increased the proportion of unreacted FA, increased the surface roughness and porosity, and decreased the strength. Yang et al. [21] used cement, tailings, and FA as raw materials to study the mechanism of FA content in cemented tailings backfill (CTB) from a molecular perspective. The addition of FA initially increased the strength of CTB and then decreased. FA strengthens the silicon chain of C-S-H and improves the strength of the matrix. However, excessive FA weakens this strengthening effect. Cheng et al. [22] studied the workability and mechanical properties of backfill under different FA/coal bottom ash (CBA) ratios using raw materials, such as cement, FA, and CBA. As the FA/CBA ratio increased, the strengths of the early and final stages decreased and increased, respectively. When the ratio of FA/CBA was greater than 50%, the strength decreased. Wang et al. [23] used cement, tailings, and FA as raw materials to study the effects of FA content and curing time on the mechanical strength of CTB. As the FA content increased, the UCS of CTB first increased and then decreased, and the elastic modulus of CTB at different ages first increased and then decreased.

The above studies mainly focus on the influence of the ratio of FA to cement on the mechanical properties of CPB materials. When river sand (RS) is added to the CPB material, in the process of hydration of materials, FA cannot only participate in the hydration reaction to generate hydration products such as C-S-H but also play a role in filling the voids of RS and increasing the strength of CPB. FA and RS have a coupling effect during the interaction. Therefore, FA and RS are studied as a whole to explore the interaction between the two and their further effects on CPB intensity. In this study, CPB was prepared with cement, CG, FA, RS, and water as raw materials. Through uniaxial compression and SEM tests, the effects of different FA and RS ratios on the mechanical properties and microstructure of CPB were studied, and the damage constitutive model of CPB was established.

2. Materials and Methods

2.1. Test Materials. In this study, the CPB sample was prepared with P.O42.5 ordinary Portland cement (OPC), CG, FA, RS, and water. OPC was obtained from a cement factory in Xuzhou City, and its main mineral components were plagioclase, gypsum, calcite, potassium feldspar, and kaolinite. The main chemical components of OPC were CaO, SiO_2, and Al_2O_3. CG was collected from a mine in Shaanxi Province, and its main mineral composition was quartz, illite, kaolinite, and pyrite. The particle size of CG was 5–10 mm, and the main chemical compositions were SiO_2, Al_2O_3, and CaO. FA was obtained from a coal-fired power plant in Shaanxi Province. The main mineral components of FA were mullite and quartz, and its main chemical components were SiO_2, Al_2O_3, and CaO [24]. RS was obtained from the Yellow River basin. The main mineral components were quartz, feldspar, calcite, and illite, and its main chemical components were SiO_2 and Al_2O_3 [25]. Table 1 shows the RS gradation [24]. Ordinary tap water was used for the experiment. Table 2 shows the chemical composition of the material.

Table 1: Grading table of river sand, in weight %.

Particle size (mm)	2–4.75	1.5–2	1–1.5	<1	Total
Percentage	3%	4%	9%	84%	100%

2.2. Sample Preparation. After many tests, the CPB ratio was determined to be OPC : FA + RS : CG: water, which is 1 : 4 : 2 : 1.2 [26]. The solid mass concentration was maintained at 85%, which met the requirements of coal mine backfill with a slump greater than 150 mm [27–29]. The test was divided into four groups according to the proportion of FA to the total mass of FA and RS: 0%, 20%, 40%, and 60%. Each group produced nine samples, each age of three samples, a total of 36 samples. The grouping and matching are shown in Table 3. After the material was configured, it was stirred with a blender and poured into a mold of 100 mm × 100 mm × 100 mm. After the sample was stored at room temperature for 24 hr, it was demolded, and the sample number was expressed by combining letters and numbers. Taking F0.2–4 as an example, "F0.2" indicates that the content of FA accounts for 20% of the total mass of FA and RS, and "4" indicates the fourth sample with the same ratio. The demolded CPB samples were placed in the standard constant temperature and humidity curing room for constant temperature and humidity curing. The curing temperature was 20 ± 2°C, and the relative humidity was greater than 95% [30].

2.3. Uniaxial Compression Test. An Mechanical Testing and Simulation (MTS) electrohydraulic servo universal testing machine was used as a uniaxial compression test instrument. The test loading mode was displacement control mode, and the loading rate was 0.6 mm/min. The samples were tested at 7, 14, and 28 days after curing. Three samples were tested in the same group at each age.

2.4. SEM Test. The microstructure of CPB was examined using SEM (VEGA 4, TESCAN). The cured sample was placed into a drying oven at 40°C to dry, and the sample with a flat surface was cut from the inside. Then, the sample was glued to the test tray using a conductive adhesive. In addition, the sample was sprayed with gold to improve its electrical conductivity for easy observation. Finally, the sample and test tray were tested. The specific test process is shown in Figure 1.

Table 2: Chemical composition of raw materials, in weight %.

Raw materials	SiO_2	Al_2O_3	K_2O	Fe_2O_3	CaO	MgO	Na_2O	Others
OPC	16.54	17.16	0.11	10.12	49.46	1.03	0.57	5.01
CG	40.36	24.3	0.94	4.97	22.7	—	—	6.73
FA	47.24	16.49	0.19	12.4	9.73	1.88	0.95	11.12
RS	65.6	12.33	3.01	2.55	3.26	1.59	1.12	10.54

Table 3: Experimental scheme design (mass ratio).

Groups	OPC	FA	RS	CG	Water
F0	1	0	4	2	1.2
F0.2	1	0.8	3.2	2	1.2
F0.4	1	1.6	2.4	2	1.2
F0.6	1	2.4	1.6	2	1.2

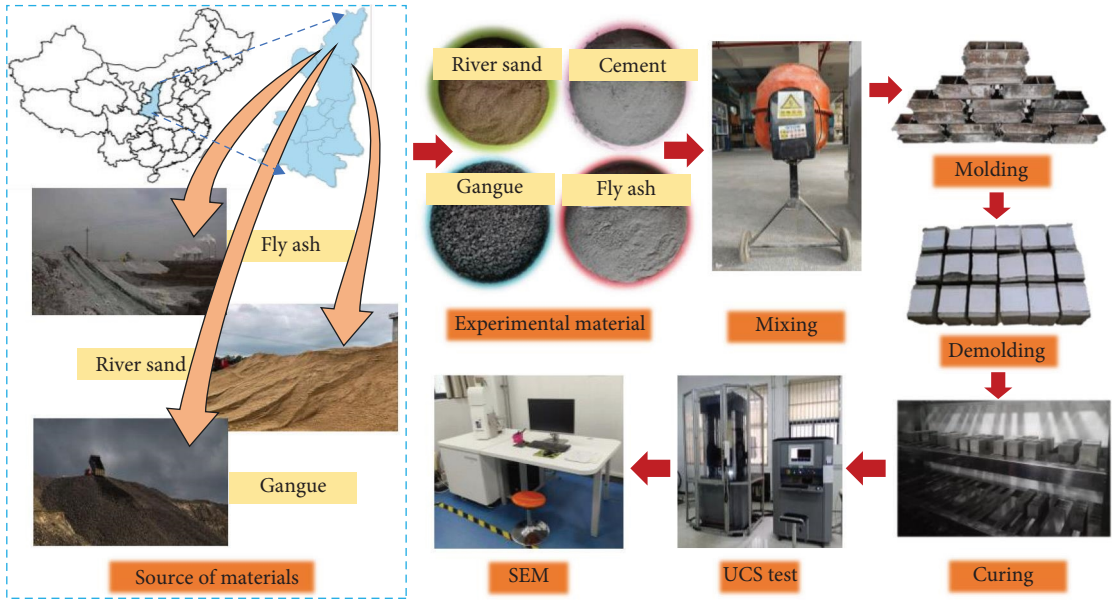

Figure 1: The experimental procedure in this study.

3. Results and Discussion

3.1. Analysis of Strength Characteristics at Different Ages. The UCS of samples at different ages was measured, and the results are shown in Table 4. The UCS of the sample at each age was averaged, and the change law of UCS of CPB with different proportions of FA at different ages is shown in Figure 2.

As shown in Figure 2(a), as the curing time increased, the UCS of materials with the same proportion increased, and the UCS growth from 7 to 14 days was greater than that from 14 to 28 days. The CPB sample achieved its optimal strength at 14 days of curing. When the content of FA in CPB was 0%, the UCS grew from 7 to 14 days. At 14 days, UCS was 1.80 MPa, which increased by 29.17%. The UCS growth from 14 to 28 days was 0.88 MPa, which increased by 11.04%. When the content of FA was 20%, the UCS growth from 7 to 14 days was 4.44 MPa, which increased by 68.10%, and the UCS growth from 14 to 28 days was 0.56 MPa, which increased by 5.09%. When the content of FA was 40%, UCS growth from 7 to 14 days was 6.04 MPa, representing an 86.66% increase, and the increase in UCS from 14 to 28 days was 1.75 MPa, representing a 13.45% increase. When the content of FA was 60%, the UCS growth from 7 to 14 days was 4.06 MPa, representing a 49.32% increase, and the UCS growth from 14 to 28 days was 0.86 MPa, representing a 6.52% increase. As the content of FA increased from 0% to 60%, the UCS of the sample gradually increased at the same time, indicating the strength generation speed was accelerated. However, when the content of FA was 60%, the UCS growth from 7 to 14 days was lower than that of the F0.2 and F0.4 groups, while that from 14 to 28 days was lower than that of the F0.4 and F0 groups. In the early stage of the sample (7 days), the hydration reaction was mainly participated by cement, and the hydration reaction of FA was followed (7–14 days). Due to the constant content of cement, the strength of the sample is not much different at 7 days, and the

Table 4: UCS of uniaxial compression test at different ages.

Groups	UCS of 7 days (MPa)	Average UCS of 7 days (MPa)	Groups	UCS of 14 days (MPa)	Average UCS of 14 days (MPa)	Groups	UCS of 28 days (MPa)	Average UCS of 28 days (MPa)
F0-1	6.72		F0-4	8.23		F0-7	9.16	
F0-2	6.27	6.17	F0-5	8.45	7.97	F0-8	9.19	8.85
F0-3	5.52		F0-6	7.23		F0-9	8.21	
F0.2-1	7.31		F0.2-4	10.54		F0.2-7	11.00	
F0.2-2	6.94	6.52	F0.2-5	10.78	10.96	F0.2-8	11.63	11.52
F0.2-3	5.31		F0.2-6	11.56		F0.2-9	11.92	
F0.4-1	7.64		F0.4-4	13.97		F0.4-7	15.14	
F0.4-2	6.73	6.97	F0.4-5	12.94	13.01	F0.4-8	13.69	14.76
F0.4-3	6.54		F0.4-6	12.12		F0.4-9	15.46	
F0.6-1	9.67		F0.6-4	12.35		F0.6-7	13.47	
F0.6-2	8.46	8.84	F0.6-5	12.13	13.20	F0.6-8	12.86	14.06
F0.6-3	8.39		F06-6	15.12		F0.6-9	15.86	

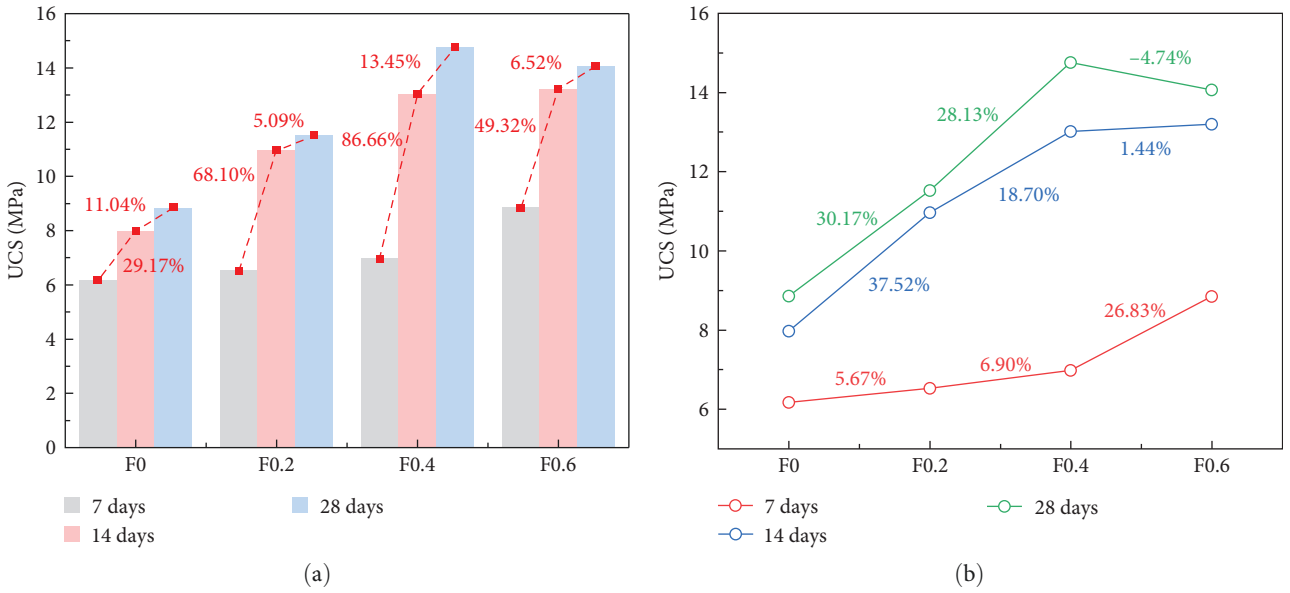

Figure 2: Average UCS of CPB with different proportions of FA. (a) UCS comparison of CPB samples of the same group at 7, 14 and 28 days; (b) UCS comparison between CPB samples of different groups at 7, 14 and 28 days.

strength of the sample is positively correlated with the FA content at 14 days. There was no obvious pattern in the strength growth of the sample from 14 to 28 days, and it only increased significantly when the FA content was 40%.

As shown in Figure 2(b), the changes in UCS of CPB samples at different ages varied with the change in FA content. After 7 days of curing, the UCS of the sample increased by 0.35, 0.45, and 1.87 MPa, with the increasing content of FA by 5.67%, 6.90%, and 26.83%, respectively. When the FA content was between 20% and 30%, the UCS of the backfill sample significantly enhanced, while when the FA content was between 0% and 40%, the UCS of the CPB sample remained unchanged. FA slightly enhanced the UCS at the early stage (7 days) of the CPB sample. However, when the content of FA was in excess in the sample, the enhancement effect became significant.

After 14 days of curing, the UCS of CPB samples increased by 2.99, 2.05, and 0.19 MPa, as the FA content increased, and the UCS of CPB increased by 37.52%, 18.70%, and 1.44%, respectively. The increase in UCS of samples was consistent before reaching the 40% FA content, and the UCS in samples remained unchanged from 40% to 60%. The enhancement effect of FA ratio on CPB samples was significant from 7 to 14 days. However, the enhancement effect disappeared when excessive FA (60%) was added to the sample.

After 28 days of curing, as FA content increased, the UCS of CPB samples increased by 2.67, 3.24, and −0.70 MPa, which increased by 30.17%, 28.13%, and −4.74%, respectively. The appropriate increase in FA content significantly enhanced the UCS of CPB samples. However, the enhancing effect diminished as FA content increased. When the content of FA was 60%, the UCS of the CPB sample decreased compared with other groups. It may be due to the fact that excessive FA hinders the progress of hydration products, and the material produces fewer hydration products. Given the enhanced UCS of CPB at 28 days, the optimal proportion of FA was about 40%.

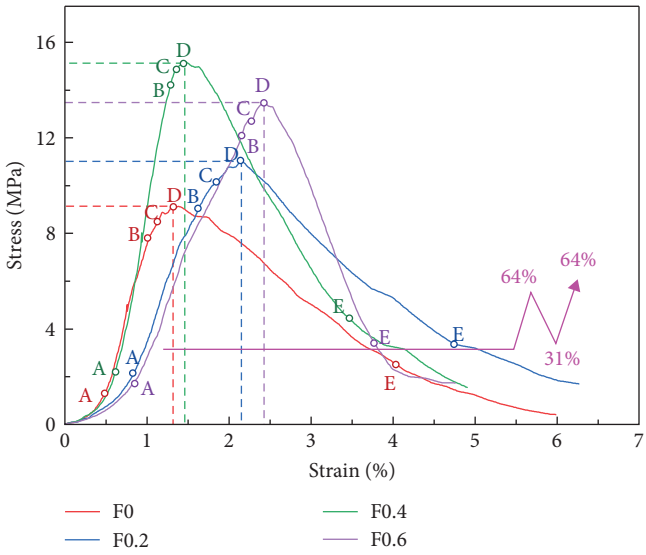

Figure 3: Stress–strain curves of CPB samples with different FA proportions.

3.2. Stress–Strain Curve Analysis. The CPB sample cured for 28 days was taken as the research object, and the stress–strain curve is shown in Figure 3. The stress–strain curves of the samples were divided into five stages: pore compaction, linear elastic deformation, elastoplastic deformation, progressive rupture, and postrupture.

In the pore compaction stage (OA), the curve of this stage is concave, the coupling degree of different components in the sample is limited, and there are some microcracks and micropores. In the process of uniaxial compression, these microcracks and micropores are gradually compressed and closed. Due to the change in FA content, the porosity of CPB samples was different. The curves of the F0 and F0.4 groups were similar at this stage, while the deformation of F0.2 and F0.6 was larger.

In the online elastic deformation stage (AB), the CPB sample transforms from a discontinuous medium to a continuous medium after the compaction stage under continuous load. As the load increases, the stress–strain curve at this stage is nearly linear. This stage is mainly due to the difference in hydration products and material density, resulting in different elastic modulus of the sample.

The F0.4 group exhibits a steep slope, indicating strong resistance to deformation. The slope of the other groups is at the same level, assuming that the slope at this stage is the elastic modulus of the material, the elastic modulus of F0.4 is significantly enhanced, and the FA ratio of the other groups has little influence on the elastic modulus.

In the elastoplastic deformation stage (BC), a new microfracture begins to occur inside the CPB sample, but the propagation speed of the fracture is relatively slow and stable, so this stage is also called the stable development stage of microfracture.

In the progressive fracture stage (CD), the elastoplastic deformation of the CPB sample starts from point C to plastic deformation and ends at point D. Point C is the yield point of the material, and the corresponding stress is called the yield stress. Point D is the complete rupture point of the material, and the corresponding stress and strain are the peak strength and peak strain, respectively. In this stage, the development of microfracture enters a state of rapid propagation, and the strain rate increases significantly. Because fracture development in this stage is extremely unstable, this stage can also be called the development stage of unstable fracture. Compared with the four groups of curves, as FA content increased, the peak stress of the CPB sample first increased and then decreased; the peak stress of F0.4 was the highest, and the peak strain initially increased, then decreased, and finally increased.

In the postfracture stage (DE), the stress–strain curve shows a strain-softening phenomenon in which the stress decreases with the increase in strain. When the CPB sample reached the peak bearing capacity at point D, its internal structure was destroyed, but the sample maintained its integrity. Cracks in the sample continue to develop after point D, and cracks in the forms of the cross, joint, penetration, and combination appear in different degrees, forming macroscopic or microscopic fracture planes. The development of cracks stops at point E. Point E is called the complete failure point, and the stress corresponding to this point is the residual strength of the material. This stage indicated that CPB samples did not immediately lose bearing capacity after reaching the strength limit but showed different degrees of postpeak bearing capacity. Due to the change in FA content, the toughness of the specimen is different, and the material with low strength shows high toughness. It is worth noting that there is little difference in the residual strength of the sample, and the law of residual strain and peak strain is different; the relationship between peak strain is F0 < F0.4 < F0.2 < F0.6, and the relationship between residual strain is F0.4 < F0.6 < F0 < F0.2.

3.3. Analysis of Elastic Modulus of Different Proportions of FA during 28 Days Curing. The elastic modulus of CPB reflects its ability to resist deformation under compression conditions. Twenty-eight days is considered to be the standard curing age in cement-based materials. According to the national standard GB 50010-2010, cement-based materials have reached 95% of the final mechanical properties at 28 days of curing age. Therefore, the elastic modulus of the material at 28 days has basically reached the final elastic modulus of the material. At the same time, when the backfill material is used in coal mine backfill, we focus on the long-term (28 days) deformation resistance of the material, so the sample of 28 days is selected for the study of elastic modulus. The slope of the sample in the online elastic deformation stage was taken as the elastic modulus of CPB.

Figure 4 shows the elastic modulus of the sample at 28 days and the mean value of the elastic modulus of different ratios. The average value was taken as the research object. The elastic modulus of the backfill sample is affected by various factors such as raw material properties, particle type, porosity, and compactness. As the FA content increased, the elastic modulus of the CPB sample first decreased, then increased, and finally decreased. The elastic modulus of F0, F0.2, F0.4, and F0.6

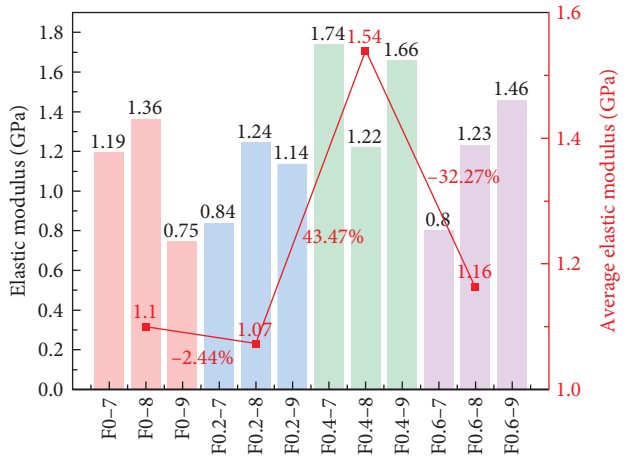

Figure 4: Elastic modulus of CPB sample after curing for 28 days.

increased by −2.44%, 43.47%, and −32.27%, respectively. The elastic modulus of the F0.4 group was the highest, with an average of 1.54 GPa. The average elastic modulus of F0, F0.2, and F0.6 were 1.1, 1.07, and 1.16 GPa, respectively. The analysis above revealed that the elastic modulus of the CPB sample containing 40% FA was significantly enhanced, while in most cases, the elastic modulus of the CPB sample did not significantly change. FA can promote the formation of hydration products and enhance the cementation effect between particles, but excessive FA can hinder the hydration reaction and cause the opposite effect. At the same time, excessive FA will lead to a decrease in the proportion of RS, which will damage the matrix properties of the material.

3.4. Microstructure Analysis. SEM was used to examine the microstructure of CPB samples at 28 days (Figure 5). Cement in contact with water will undergo hydration reactions to form colloidal calcium silicate hydrate (C-S-H) and flake calcium hydroxide (C-H), and gypsum in cement will form ettringite (Aft) with tricalcium aluminate hydrate [31]. As the hydration reaction progressed, C-H generated by cement hydration stimulated and accelerated the volcanic ash reaction of FA, which led to gradual breakage of the surface of FA to form C-S-H and hydrated calcium aluminate (C-A-H) [32]. Hydration products, such as C-S-H, bound the components together and strengthened the material. According to the 300x magnification of Figure 5(a)–5(d), as the FA content increased in the sample, spherical FA particles optimized the particle size gradation of the material, filled the microholes and microcracks of the material [20], and reduced the porosity of the CPB sample, making the surface denser. Figure 5(e)–5(g) shows that as the FA increases, hydration products increase, and the bond between particles becomes closer, which is the fundamental reason for improving CPB strength. However, numerous unreacted FA particles can be seen in Figure 5(h), with large pores between component particles. Because FA particles are smaller than cement particles, they are easy to adhere to the surface of cement particles, inhibiting the hydration reaction and hindering the generation of hydration products. Therefore, excessive FA reduces the strength of CPB [23].

4. CPB Damage Constitutive Models with Different FA Content

4.1. Establishment of Damage Constitutive Model. In the uniaxial compression process, the damage degree can be used to represent the damage evolution of the material. Assuming that the specimen continuously develops failure at each stage, the damage constitutive equation is established according to the Lemaitre strain equivalence principle as follows [33–35]:

$$\sigma' = \sigma(1 - D) = E\varepsilon(1 - D), \tag{1}$$

where σ' is the effective stress, σ is the nominal stress, that is, the stress of the material during the experiment, E is the elastic modulus of the material, which can be replaced by the initial elastic modulus of the material E_0, ε is the material strain, and D is the damage variable.

The failure process of the sample is regarded as the failure of the microelement body, and the failure probability of the sample microelement body is represented by Weibull distribution, which can be expressed as follows [36, 37]:

$$P(F) = \frac{\beta}{\mu}\left(\frac{F}{\mu}\right)^{\beta-1}\exp\left[-\left(\frac{F}{\mu}\right)^{\beta}\right], \tag{2}$$

where β and μ are Weibull distribution parameters, and F is the sample strength distribution variables.

Assuming that the area number of destroyed microelements in a certain section of the sample under load is S_{Dn}, the damage variable D is defined as the ratio of the area number of destroyed microelements to the total area number of microelements S_n, namely

$$D = S_{Dn}/S_n. \tag{3}$$

In any interval $(F, F + dF)$, the area number of destroyed microelements is $S_nP(D_n)dD_n$. When the load is loaded to a certain level F, the area number of destroyed microelements is as follows:

$$S_{Dn}(F) = \int_0^F S_nP(Dn)dDn = S_n\left\{1 - \exp\left[-\left(\frac{F}{\mu}\right)^{\beta}\right]\right\}. \tag{4}$$

By substituting Equation (4) into Equation (3), the damage variable can be obtained as follows:

$$D = S_{Dn}/S_n = 1 - \exp\left[-\left(\frac{F}{\mu}\right)^{\beta}\right], \tag{5}$$

where the F value is the strength distribution variable of the cell, different physical values can be used according to the needs of damage models. In uniaxial compression tests, the failure process of samples containing fiber is mainly caused by local tension and shear, and the whole process of sample failure

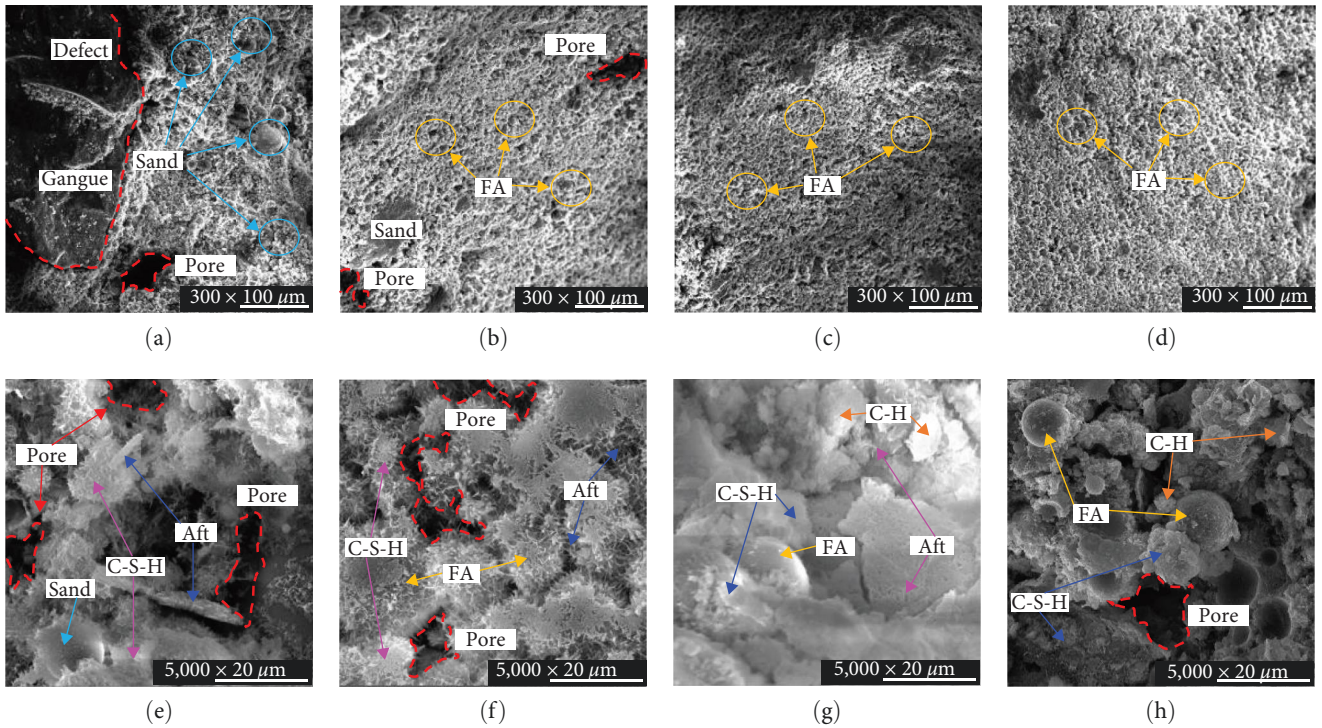

Figure 5: Microstructure of samples with different proportions: (a)–(d) are images of 300x F0–F0.6 magnification; (e)–(h) is an image magnified by 5,000 times F0–F0.6.

can be better described using the physical quantity of material strain. The damage evolution equation using strain is as follows:

$$D = 1 - \exp\left[-\left(\frac{\varepsilon}{\mu}\right)^{\beta}\right]. \tag{6}$$

By substituting Equation (6) into Equation (1), we get the following:

$$\sigma = \varepsilon E(1 - D) = \varepsilon E_0 \exp\left[-\left(\frac{\varepsilon}{\mu}\right)^{\beta}\right]. \tag{7}$$

The boundary conditions of the sample obtained from the stress–strain curve are as follows:

$$\begin{cases} \varepsilon = 0 \\ \sigma = 0 \end{cases}, \tag{8}$$

$$\begin{cases} \varepsilon = \varepsilon_m \\ \sigma = \sigma_m \end{cases}, \tag{9}$$

$$\begin{cases} \left.\dfrac{d\sigma}{d\varepsilon}\right|_{\varepsilon=\varepsilon_m} = 0 \\ \left.\dfrac{d\sigma}{d\varepsilon}\right|_{D=0} = E_0 \end{cases}, \tag{10}$$

where ε_m is the peak strain and σ_m is the peak stress.

Simultaneous equations can be obtained as follows:

$$\beta = \frac{1}{\ln\left(\frac{E_0\varepsilon_m}{\sigma_m}\right)}, \tag{11}$$

$$\mu = \frac{\varepsilon_m}{(1/\beta)^{1/\beta}}, \tag{12}$$

$$D = 1 - \exp\left[-\frac{1}{\beta}\left(\frac{\varepsilon}{\varepsilon_m}\right)^{\beta}\right], \tag{13}$$

$$\sigma = E_0\varepsilon \exp\left[-\frac{1}{\beta}\left(\frac{\varepsilon}{\varepsilon_m}\right)^{\beta}\right]. \tag{14}$$

4.2. Modification of Damage Constitutive Model. To accurately simulate the stress–strain process before the peak of CPB samples with different contents of FA and RS, the logarithmic function of strain was used as the prepeak correction coefficient α [38]. The expression of α is shown in Equation (15); when the strain of the sample reaches the peak strain ε_m, the value of α is 1.

$$\alpha = \begin{cases} \log_{\omega}\left[\dfrac{(\omega - 1)\varepsilon}{\varepsilon_m} + 1\right], & \varepsilon < \varepsilon_m \\ 1, & \varepsilon \geq \varepsilon_m \end{cases}, \tag{15}$$

where ω is the constant obtained by fitting experimental data. The prepeak correction factor α is the ratio of the slope

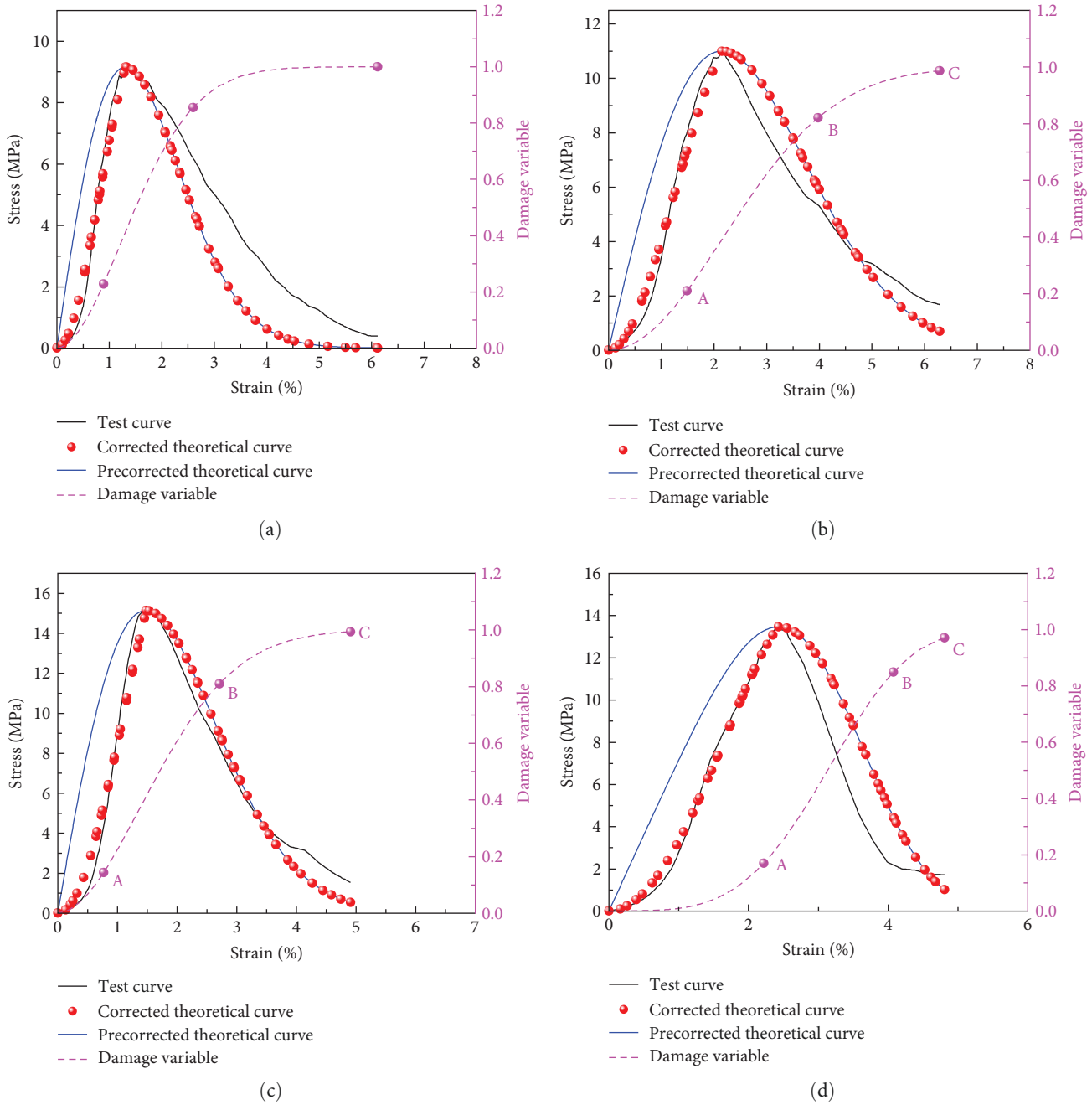

Figure 6: Test curve, theoretical curve, and damage curve: (a) F0; (b) F0.2; (c) F0.4; (d) F0.6.

of the stress–strain curve and elastic modulus of CPB samples with different proportions of FA, and its value increases in the form of a logarithmic function. By substituting the correction coefficient into Equation (14) to obtain a modified constitutive model as follows:

$$\sigma = \begin{cases} \log_{\omega}\left[\dfrac{(\omega-1)\varepsilon}{\varepsilon_m}+1\right]E_0\varepsilon\exp\left[-\dfrac{1}{\beta}\left(\dfrac{\varepsilon}{\varepsilon_m}\right)^{\beta}\right], & \varepsilon<\varepsilon_m \\ E_0\varepsilon\exp\left[-\dfrac{1}{\beta}\left(\dfrac{\varepsilon}{\varepsilon_m}\right)^{\beta}\right], & \varepsilon\geq\varepsilon_m \end{cases}. \tag{16}$$

4.3. Damage Evolution and Constitutive Model Verification. As shown in Figure 6, the damage curve of the CPB sample can be divided into three stages. The OA stage is the initial damage stage, in which the pores and cracks in the material are compacted before entering the elastic deformation stage. As the strain increases, the damage development speed is accelerated, and the final sample of this stage reaches the elastic limit. The AB stage represents the damage stable development stage, and the damage growth rate tends to be stable at this stage, corresponding to the plastic deformation stage and the progressive postpeak fracture stage of the sample. The microcrack growth rate in the sample is relatively stable at this stage. The BC stage represents the residual damage stage, corresponding to the postrupture stage of the sample. In this stage, the damage development rate retards, the damage tends to a fixed value, the sample is completely destroyed, and the residual strength is low.

The classical constitutive model (Equation (14)) largely deviated from the test curve in the prepeak stage. However, the revised constitutive model (Equation (16)) could be used to solve this problem. The modified curve was consistent with the peak strength of the test curve, but there was a slight deviation in the postpeak stage, and the overall fit of the curve was high. The modified model curve can better reflect the variation of the stress–strain curve of the sample under load.

5. Conclusions

In this study, the effects of different FA and RS ratios on the peak strength, elastic modulus, and microstructure of CPB were studied using uniaxial compression and SEM tests. The following findings were obtained from this study:

(1) As the FA content in CPB increased, UCS at 7 and 14 days of CPB gradually increased, while UCS at 28 days initially increased and then decreased. When the content of FA was 40%, the UCS of CPB at 28 days reached the maximum value of 14.76 MPa.

(2) As FA content increased, the elastic modulus of CPB first decreased, then increased, and finally decreased. When FA content in CPB was 40%, the elastic modulus reached its highest value of 1.54 GPa.

(3) The incorporation of FA improved particle gradation, filled the pores between particles, reduced porosity, promoted the generation of hydration products, and thus increased CPB strength. When the content of FA exceeded 40%, the number of unreacted FA particles increased, thus inhibiting the generation of hydration products and increasing the porosity of the material, thereby deteriorating CPB strength.

(4) Based on Weibull distribution, the damage constitutive model of CPB was constructed by introducing the prepeak correction factor, and the logarithmic function of strain was used to modify the model prepeak. The modified model better described the whole stress–strain curve process of CPB under load. This model will provide a theoretical reference for CPB design.

Data Availability

The data used to support the findings of this study are available from the corresponding author upon request.

Conflicts of Interest

The authors declare that there are no conflicts of interest regarding the publication of this paper.

Acknowledgments

This work was supported by the National Natural Science Foundation of China (grant nos. 52274143 and 51874284).

References

[1] D. Wu, R.-K. Zhao, C.-W. Xie, and S. Liu, "Effect of curing humidity on performance of cemented paste backfill," *International Journal of Minerals, Metallurgy and Materials*, vol. 27, no. 8, pp. 1046–1053, 2020.

[2] W. Guo, G. Zhao, E. Bai, M. Guo, and Y. Wang, "Effect of overburden bending deformation and alluvium mechanical parameters on surface subsidence due to longwall mining," *Bulletin of Engineering Geology and the Environment*, vol. 80, no. 3, pp. 2751–2764, 2021.

[3] Y. Sun, J. Zuo, M. Karakus, L. Liu, H. Zhou, and M. Yu, "A new theoretical method to predict strata movement and surface subsidence due to inclined coal seam mining," *Rock Mechanics and Rock Engineering*, vol. 54, no. 6, pp. 2723–2740, 2021.

[4] B. Yan, H. Jia, Z. Yang, E. Yilmaz, and H. Liu, "Goaf instability in an open pit iron mine triggered by dynamics disturbance: a large-scale similar simulation," *International Journal of Mining, Reclamation and Environment*, vol. 37, no. 8, pp. 606–629, 2023.

[5] Y. Xue, S. Liu, J. Chai et al., "Effect of water-cooling shock on fracture initiation and morphology of high-temperature granite: application of hydraulic fracturing to enhanced geothermal systems," *Applied Energy*, vol. 337, Article ID 120858, 2023.

[6] Y. Xue, P. G. Ranjith, F. Gao, Z. Zhang, and S. Wang, "Experimental investigations on effects of gas pressure on mechanical behaviors and failure characteristic of coals," *Journal of Rock Mechanics and Geotechnical Engineering*, vol. 15, no. 2, pp. 412–428, 2023.

[7] Y. Zhang, Y. Liu, X. Lai et al., "Transport mechanism and control technology of heavy metal ions in gangue backfill materials in short-wall block backfill mining," *Science of The Total Environment*, vol. 895, Article ID 165139, 2023.

[8] H. Gao, Y. Huang, W. Li et al., "Explanation of heavy metal pollution in coal mines of China from the perspective of coal gangue geochemical characteristics," *Environmental Science and Pollution Research*, vol. 28, pp. 65363–65373, 2021.

[9] Z. Xu, Y. Qian, X. Hong, Z. Luo, X. Gao, and H. Liang, "Contamination characteristics of polycyclic aromatic compounds from coal sources in typical coal mining areas in Huaibei area, China," *Science of The Total Environment*, vol. 873, Article ID 162311, 2023.

[10] W. Song, J. Zhang, M. Li et al., "Underground disposal of coal gangue backfill in China," *Applied Sciences*, vol. 12, no. 23, Article ID 12060, 2022.

[11] A. Wu, Z. Ruan, and J. Wang, "Rheological behavior of paste in metal mines," *International Journal of Minerals, Metallurgy and Materials*, vol. 29, no. 4, pp. 717–726, 2022.

[12] X. Liu, "Low-carbon utilization of coal gangue under the carbon neutralization strategy: a short review," *Journal of Material Cycles and Waste Management*, vol. 25, no. 4, pp. 1978–1987, 2023.

[13] S. Cao, G. Xue, E. Yilmaz, Z. Yin, and F. Yang, "Utilizing concrete pillars as an environmental mining practice in underground mines," *Journal of Cleaner Production*, vol. 278, Article ID 123433, 2021.

[14] Y. Feng, W. Qi, Q. Zhao et al., "Synthesis and characterization of cemented paste backfill: reuse of multiple solid wastes," *Journal of Cleaner Production*, vol. 383, Article ID 135376, 2023.

[15] N. Zhou, H. Ma, S. Ouyang, D. Germain, and T. Hou, "Influential factors in transportation and mechanical properties of aeolian sand-based cemented filling material," *Minerals*, vol. 9, no. 2, Article ID 116, 2019.

[16] B. Yan, H. Jia, E. Yilmaz, X. Lai, P. Shan, and C. Hou, "Numerical study on microscale and macroscale strength behaviors of hardening cemented paste backfill," *Construction and Building Materials*, vol. 321, Article ID 126327, 2022.

[17] G. Feng, W. Liu, X. Du, J. Wang, X. Li, and Y. Zheng, "Crack evolution characteristics of cemented-gangue-fly-ash backfill with different proportions of fly ash and cement," *Construction and Building Materials*, vol. 385, Article ID 131498, 2023.

[18] S. Yin, Z. Yan, X. Chen, and L. Wang, "Effect of fly-ash as fine aggregate on the workability and mechanical properties of cemented paste backfill," *Case Studies in Construction Materials*, vol. 16, Article ID e01039, 2022.

[19] Q. Sun, S. Tian, Q. Sun et al., "Preparation and microstructure of fly ash geopolymer paste backfill material," *Journal of Cleaner Production*, vol. 225, pp. 376–390, 2019.

[20] J.-X. Fu, K. Wang, and J. Wang, "Internal pore evolution and early hydration characterization of fly ash cement backfill," *Journal of Building Engineering*, vol. 72, Article ID 106716, 2023.

[21] S. Yang, J. Wu, H. Jing et al., "Molecular mechanism of fly ash affecting the performance of cemented backfill material," *International Journal of Minerals, Metallurgy and Materials*, vol. 30, no. 8, pp. 1560–1572, 2023.

[22] B. Cheng, R. Liu, X. Li, E. del Rey Castillo, M. Chen, and S. Li, "Effects of fly and coal bottom ash ratio on backfill material performance," *Construction and Building Materials*, vol. 319, Article ID 125831, 2022.

[23] Y. Wang, J. Wu, D. Ma, H. Pu, Q. Yin, and W. Chen, "Study on macro-meso mechanical properties of cemented tailings backfill with high fly ash content," *Environmental Science and Pollution Research*, vol. 30, no. 2, pp. 2904–2917, 2023.

[24] S. Zhang, C. Che, C. Zhao et al., "Effect of fly ash and steel fiber content on workability and mechanical properties of roadway side backfilling materials in deep mine," *Energies*, vol. 16, no. 3, Article ID 1505, 2023.

[25] N. Zhou, J. Zhang, S. Ouyang, X. Deng, C. Dong, and E. Du, "Feasibility study and performance optimization of sand-based cemented paste backfill materials," *Journal of Cleaner Production*, vol. 259, Article ID 120798, 2020.

[26] J. Li, *Research and application of bearing characteristics of strong-toughness cemented backfilling materials*, M. S. thesis, China University of Mining and Technology, Xuzhou, China, 2021.

[27] C. Che, S. Cao, C. Zhao, S. Du, J. Li, and Y. Liu, "Research on cemented artificial pillars to replace protective inter-block coal pillars and stope failure laws," *Frontiers in Earth Science*, vol. 10, 2023.

[28] A. Wu, Y. Wang, H. Wang, S. Yin, and X. Miao, "Coupled effects of cement type and water quality on the properties of cemented paste backfill," *International Journal of Mineral Processing*, vol. 143, pp. 65–71, 2015.

[29] D. Ouattara, T. Belem, M. Mbonimpa, and A. Yahia, "Effect of superplasticizers on the consistency and unconfined compressive strength of cemented paste backfills," *Construction and Building Materials*, vol. 181, pp. 59–72, 2018.

[30] B. Li, J. Zhang, H. Yan, H. Liu, and C. Zhu, "Thermal enhancement of gangue-cemented paste backfill with graphite and silica sand: an experimental investigation," *Environmental Science and Pollution Research*, vol. 29, no. 32, pp. 49050–49058, 2022.

[31] B. Yin, T. Kang, J. Kang, Y. Chen, L. Wu, and M. Du, "Investigation of the hydration kinetics and microstructure formation mechanism of fresh fly ash cemented filling materials based on hydration heat and volume resistivity characteristics," *Applied Clay Science*, vol. 166, pp. 146–158, 2018.

[32] S. Ouyang, Y. Huang, N. Zhou, J. Li, H. Gao, and Y. Guo, "Experiment on hydration exothermic characteristics and hydration mechanism of sand-based cemented paste backfill materials," *Construction and Building Materials*, vol. 318, Article ID 125870, 2022.

[33] J. Xu, Z. Wu, H. Chen, L. Shao, X. Zhou, and S. Wang, "Influence of dry-wet cycles on the strength behavior of basalt-fiber reinforced loess," *Engineering Geology*, vol. 302, Article ID 106645, 2022.

[34] Y. Zhou, X. Yu, Z. Guo et al., "On acoustic emission characteristics, initiation crack intensity, and damage evolution of cement-paste backfill under uniaxial compression," *Construction and Building Materials*, vol. 269, Article ID 121261, 2021.

[35] M. Deng, Z. Zhang, W. Yu, J. Xin, and S. Xu, "Acoustic emission characteristics and damage law for prefabricated single-crack sandstone under uniaxial compression," *Structural Control and Health Monitoring*, vol. 29, no. 10, 2022.

[36] K. Cheng, B. Tu, L. Liu, B. Zhang, and H. Qiu, "Damage strengthening constitutive model of cemented paste backfill," *Advances in Civil Engineering*, vol. 2021, Article ID 5593983, 10 pages, 2021.

[37] K. Zhao, Y. Zhou, Q. Huang et al., "Early properties and modeling of cemented superfine tailings backfill containing sodium dodecyl sulfate: microstructure, mechanics, and acoustics," *Mechanics of Materials*, vol. 179, Article ID 104567, 2023.

[38] S. Jin, K. Liu, J. Huang, and S. Jin, "Study on damage constitutive model of backfill under uniaxial compression loading," *Gold Science and Technology*, vol. 29, no. 4, pp. 555–563, 2021.